Supporting information for “Breaking the bandwidth barrier: Graphene-driven programmable transmissive metasurfaces enable ultra-wideband terahertz beam steering”

Supplementary Note 1 Surface impedance model of graphene

The thickness of graphene is considerably less than the wavelength of terahertz waves. Consequently, graphene is frequently characterized in the terahertz frequency range using a surface impedance model.[1], [2]

The surface impedance Z_s is given by the equation $Z_s = 1/\sigma_s$, where σ_s represents the conductivity of single-layer graphene, which is expressed as

$$\sigma_s = \sigma_s^{intra} + \sigma_s^{inter} \tag{S.1}$$

Where σ_s^{intra} is the contribution of the intraband conductivity, which accounts for the motion of charge carriers within the same energy band of graphene, and σ_s^{inter} is the interband conductivity, which arises from transitions between different energy bands of graphene. According to the Kubo's formula, the intraband and interband conductivities can be described as

$$\sigma_s^{intra}(\omega,\mu_c,\Gamma,\mathrm{T}) = -j\frac{e^2 k_B T}{\pi\hbar(\omega - j2\Gamma)}\left(\frac{\mu_c}{k_B T} + 2\ln\left(e^{-\mu_c/k_B T}+1\right)\right) \tag{S.2}$$

$$\sigma_s^{inter}(\omega,\mu_c,\Gamma,\mathrm{T}) = -j\frac{e^2}{4\pi\hbar}\left(\frac{2|\mu_c| - (\omega - j2\Gamma)\hbar}{2|\mu_c| + (\omega - j2\Gamma)\hbar}\right) \tag{S.3}$$

In the aforementioned equations, e represents the elementary charge, k_B is the Boltzmann constant, $\hbar$ is the reduced Planck's constant, ω is the angular frequency, T is the temperature (fixed at 300 K), μ_c represents the chemical potential or Fermi energy of graphene, and Γ represents the scattering rate.

In the terahertz frequency ranges, Pauli blocking occurs where the energy of incident electrons is insufficient to excite transitions from the valence band to the conduction band in graphene. In this regime, the conductivity of graphene is primarily dominated by σ_s^{intra}. Accordingly, the surface impedance of graphene can be derived as

$$Z_s = 1/\sigma_s \approx \frac{\pi\hbar(\omega - j2\Gamma)}{je^2 k_B T}\left(\frac{\mu_c}{k_B T} + 2\ln\left(e^{-\mu_c/k_B T}+1\right)\right)^{-1} \tag{S.4}$$

We conducted an analysis of the effect of the chemical potential on the surface impedance of graphene, and the simulation results are shown in Fig. S1. In the simulations, we set the relaxation time of graphene (τ) to be 40 *f*s, corresponding to $\Gamma = 1.25\times10^{13}$ Hz [3].

In the terahertz band, the real part (R_s) and the imaginary part (X_s) of the surface impedance (Z_s) of graphene exhibit an inverse relationship with increasing chemical potential. As μ_c decreases from 0.4 eV to 0 eV, R_s increases from 530 Ω/sq to 6000 Ω/sq, while X_s increases from a few tens of Ω/sq to over a hundred Ω/sq. The real part of the surface impedance remains nearly constant and shows minimal frequency dependence. Furthermore, the magnitude of the imaginary part relative to the real part is significantly smaller, with R_s dominating over X_s, making the reactance effects negligible. Consequently, it is reasonable to assume that Z_s is approximately equal to R_s. Therefore, under standard environmental conditions, graphene exhibits a uniform planar resistivity characteristic in the terahertz frequency regime.

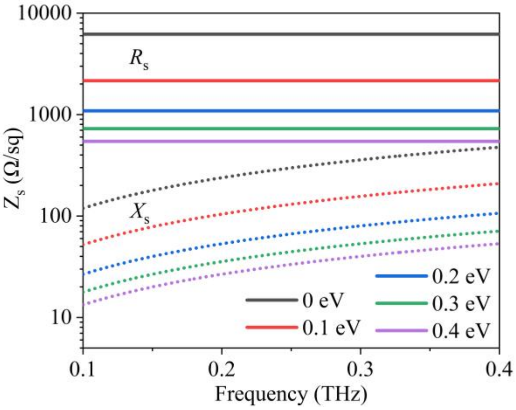

Supplementary Figure S1. The surface impedance of graphene varies with μ_c.

Supplementary Note 2 Structure of the duel-resonator unit cell

The configuration of the unit cell is illustrated in Fig. S2. The unit cell period is designated as P and comprises a metallic grating at the bottom, a quartz dielectric medium, and a circular slot at the top. Two mirror-image GIG heterostructures are positioned on the upper surface of the circular slot, designated as GIG_1 and GIG_2, with an angle 2θ between them. The bottom graphene sheet extends across both sides of the circular slot, with a 20 μm overlap width retained on each side with the electrodes. The overall length and width of the bottom graphene sheet are designated as L_g and W_g, respectively. The top graphene sheet is insulated from the bottom one, and a gate bias is provided through a gate electrode with a width of W_p. The principal structural characteristics of the unit cell are presented in Table S1.

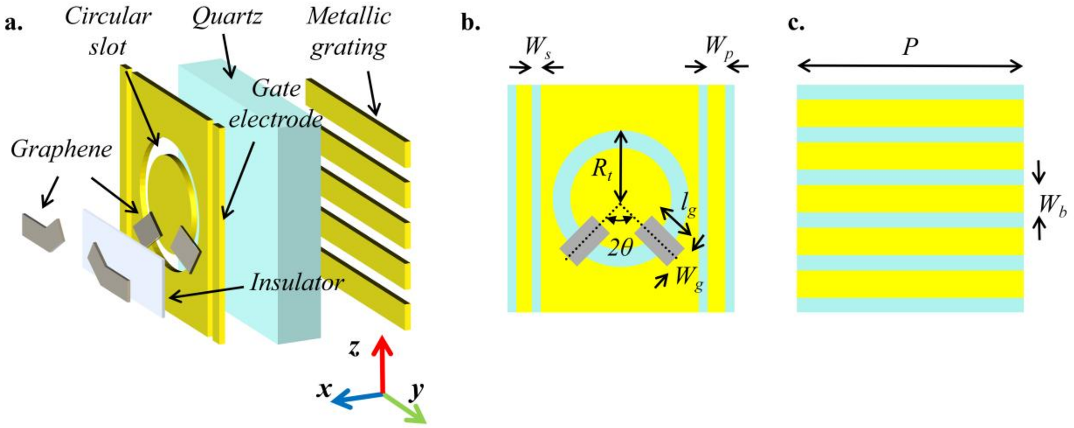

Supplementary Figure S2. a Schematic Diagram of the unit cell. **b** Top view and **c** bottom view of the unit cell.

Supplementary Table S1 Structural characteristics of the unit cell

θ	P	R_t	W_p
90°	600 μm	200 μm	30 μm
W_g	L_g	W_b	W_s
115 μm	85 μm	70 μm	20 μm

Supplementary Note 3 Transmission enhancement based on coupled mode theory

To enhance the interaction between the unit cell and terahertz waves, we have designed a dual-resonant unit cell structure. The coupled mode theory (CMT) is employed to analyze the working principle of the unit cell. According to CMT, a system can be viewed as a coupling of several modes or structures, and the various modes of a system can be represented as oscillators that interact through coupling coefficients. The transient equations of these oscillators can be solved to predict the evolution of the system over time.

Assuming there is a resonator *a*, a differential equation follows with respect to time as

$$\frac{da}{dt} = \left(j\omega_1 - \gamma_1\right)a + jq_1E \tag{S.5}$$

The symbol ω_1 represents the resonance frequency, and γ_1 represents the resonance loss. Given that the resonator must be excited by the incident electromagnetic wave in order to induce resonance, the symbol E denotes the amplitude of the electric field of the incident electromagnetic wave, while the symbol q_1 represents the coupling strength of the incident electromagnetic wave to the resonator. Consequently, the term q_1E indicates the efficiency of the electromagnetic wave in exciting the resonator, reflecting the extent to which the incident electromagnetic wave interacts with the resonator.

When two resonators are coupled, it is necessary to consider the energy exchange between the two structures. This requires the introduction of a coupling term into the equations. The transient equation can be written as:

$$\frac{da}{dt} = \left(j\omega_1 - \gamma_1\right)a + jkb + jq_1E \tag{S.6}$$

$$\frac{db}{dt} = \left(j\omega_2 - \gamma_2\right)b + jka + jq_2E \tag{S.7}$$

In the aforementioned equations, the value of k represents the coupling coefficient between resonator *a* and resonator *b*, while ω_2, γ_1, and q_2 denote the resonance frequency, resonance loss, and coupling coefficient to the incident electric field of resonator b, respectively.

Let $da/dt = j\omega a$, and $db/dt = j\omega b$, which represent that the two resonators have reached a steady state, where their amplitudes no longer change over time, the equations (S.6) and (S.7) can be express as

$$\frac{d}{dt}\begin{pmatrix} a \\ b \end{pmatrix} = \begin{pmatrix} j\omega_1 - \gamma_1 & jk \\ jk & j\omega_2 - \gamma_2 \end{pmatrix}\begin{pmatrix} a \\ b \end{pmatrix} + j\begin{pmatrix} q_1 E \\ q_2 E \end{pmatrix} = j\omega\begin{pmatrix} a \\ b \end{pmatrix} \tag{S.8}$$

After simplification, we obtain

$$\begin{pmatrix} \omega - \omega_1 - j\gamma_1 & k \\ k & \omega - \omega_2 - j\gamma_2 \end{pmatrix}\begin{pmatrix} a \\ b \end{pmatrix} = \begin{pmatrix} q_1 E \\ q_2 E \end{pmatrix} \tag{S.9}$$

By solving the above equation, we can obtain the amplitudes of resonators *a* and *b*, which are given by

$$a = \frac{q_1(\omega - \omega_2 - j\gamma_2)E - q_2 kE}{(\omega - \omega_1 - j\gamma_1)(\omega - \omega_2 - j\gamma_2) - k^2} \tag{S.10}$$

$$b = \frac{q_2(\omega - \omega_1 - j\gamma_1)E - q_1 kE}{(\omega - \omega_1 - j\gamma_1)(\omega - \omega_2 - j\gamma_2) - k^2} \tag{S.11}$$

For a dual-resonator system composed of metallic grids and slots, its transmission coefficient can be expressed as:[4]

$$T \approx 1 - \mathrm{Im}\left(\frac{q_1 a + q_2 b}{E}\right) \tag{S.12}$$

To validate the enhancement of graphene-THz wave interaction via the dual-resonator structure, we performed electromagnetic simulations using CST Microwave Studio with unit cell boundary. We approximated the graphene on the left side of the unit cell as an ideal insulator, replacing it with air. Consequently, the unit cell can be simplified to the mutual coupling of rectangular grids and C-shaped splitting ring (CSRR) resonators loaded with graphene, as illustrated in Fig. S3. In addition, the combination of a rectangular grid and a CSRR resonant structure enables the conversion of electromagnetic waves incident perpendicular to the rectangular grid into their orthogonal polarization for radiation.[5, 6]

In the simulation, it was assumed that the chemical potential of graphene, μ_c, is equal to 1 eV. Simulation results demonstrate that the dual-resonator unit cell exhibits a 25% enhancement in transmission efficiency compared to the single-CSRR configuration. This evidence suggests that by employing a reasonable design approach to the coupling between resonators, it is possible to achieve an improvement in the transmission efficiency of the unit cell.

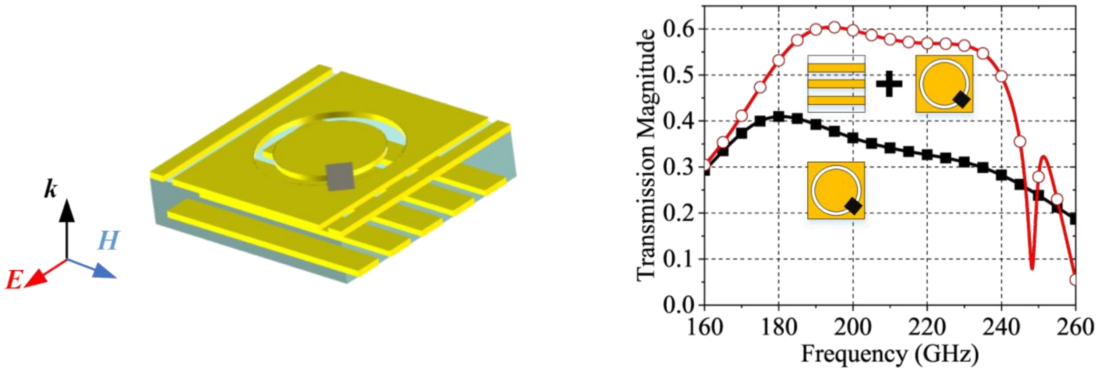

(*a*) (*b*)

Supplementary Figure S3. a Structure and **b** transmission magnitude of the dual-resonator system

Supplementary Note 4 GIG structural parameters and manufacturing process

The GIG heterostructure employed in the unit cell and its microscopic image are illustrated in Fig. S4 and Fig. S5. The bottom graphene layer is rectangular in shape, with a length and width of W_{gb} and L_{gb}, respectively. The top graphene is characterized by a V-shaped structure, with its dimensions defined by W_{gu1}, W_{gu2}, L_{gu1}, L_{gu2}, L_{gu3}, and L_{gu4}. The corresponding dimensions are listed in Table S2. The bottom graphene is in contact with the source and drain electrodes, whereas the top graphene only contacts the rectangular electrodes on each side of the unit cell that supply the gate voltage. An insulating layer with a length of L_{d} and a width of W_{d} is employed to separate the top and bottom graphene layers. In order to ensure that the impedance test results of the GIG heterostructure can directly inform the design of RF performance, the corresponding test electrode shape is designed to be similar to the actual structure used in the unit cell. The structural differences are as follows: Firstly, to facilitate the application of DC probes, the rectangular electrodes on each side of the unit cell that supply the gate voltage have been widened. Secondly, a slit has been added to the center of the unit cell, splitting the source electrode into two parts to facilitate separate testing of the GIG heterostructures on both sides.

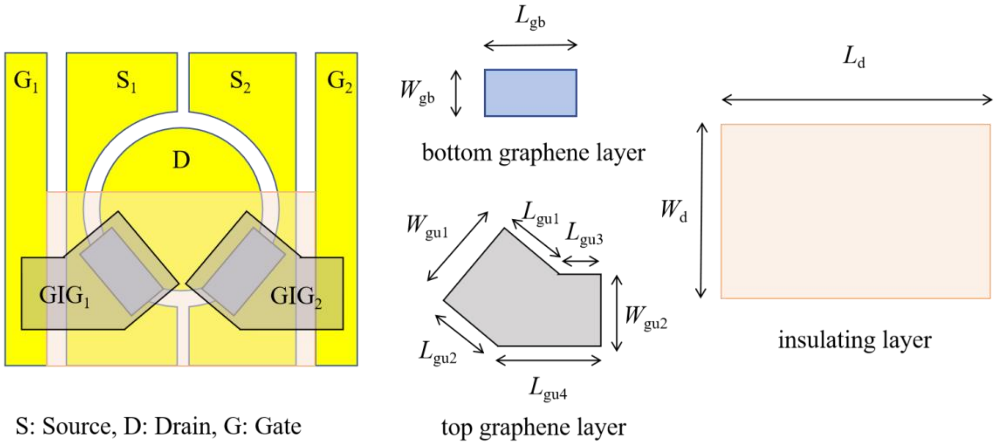

Supplementary Figure S4. Schematic diagram of the GIG heterostructure. The left side of the figure depicts the GIG heterostructure and electrodes pertinent to the surface impedance test, with the GIG heterostructures exhibiting a symmetrical distribution on both sides. The right side of the figure illustrates the structure of the bottom graphene layer, top graphene layer, and insulating layer within the GIG heterostructure.

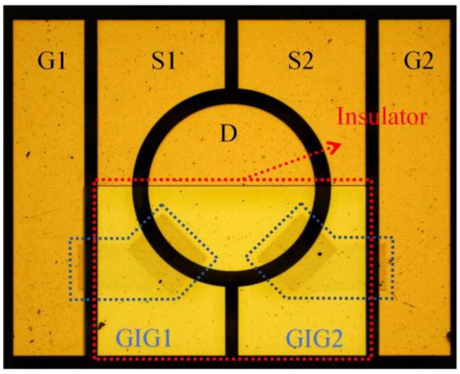

Supplementary Figure S5. The microscopic image of the GIG heterostructure adopted by the unit cell.

Supplementary Table S2. The corresponding dimensions of the GIG heterostructure. (μm)

W_{gb}	L_{gb}	W_{gu1}	W_{gu2}	L_{gu1}
95	115	115	85	80
L_{gu2}	L_{gu3}	L_{gu4}	W_d	L_d
85	92	170	300	520

The fabrication process of the GIG heterostructure and its corresponding electrodes is illustrated in Figure S6. Initially, a 5 nm thick chromium (Cr) layer is deposited on a 2-inch, 200 μm thick quartz substrate through magnetron sputtering, thereby providing a seed layer to enhance the adhesion between the gold film and the substrate. Afterward, a 40 nm gold film is grown on the Cr layer.

Subsequently, a layer of AZ6112 photoresist was spin-coated onto the gold layer at a speed of 500 r/min for 6 s, followed by 4000 r/min for 30 s. The coated substrate was then dried at 100 °C for 120 s. The photoresist was patterned using UV lithography, with the aid of a Cr-plated quartz mask. Next, the Ion Beam Etching (IBE) process was employed to remove the undesired metal structures, and a lift-off process was performed to remove excess photoresist.

The transfer and processing of GIG heterostructure were carried out by Sixcarbon Tech Shenzhen. A monolayer of graphene was synthesized using chemical vapour deposition (CVD) on copper foils and subsequently transferred onto the prepared substrate. Then, a 3 nm thick hBN layer was transferred onto the graphene film. Subsequently, the hBN-graphene heterostructure was patterned into a rectangular shape corresponding to the bottom graphene layer through laser etching. Thereafter, the atomic layer deposition (ALD) process was employed to deposit 30 nm of SiO_2 and 45 nm of Al_2O_3 at a temperature of 150 °C. Subsequently, photolithography is employed to pattern the insulating layer to the requisite dimensions. Thereafter, a monolayer of graphene and a 3 nm-thick hBN film are transferred onto the insulating layer. Finally, a laser etching process is employed to pattern the graphene-hBN composite film.

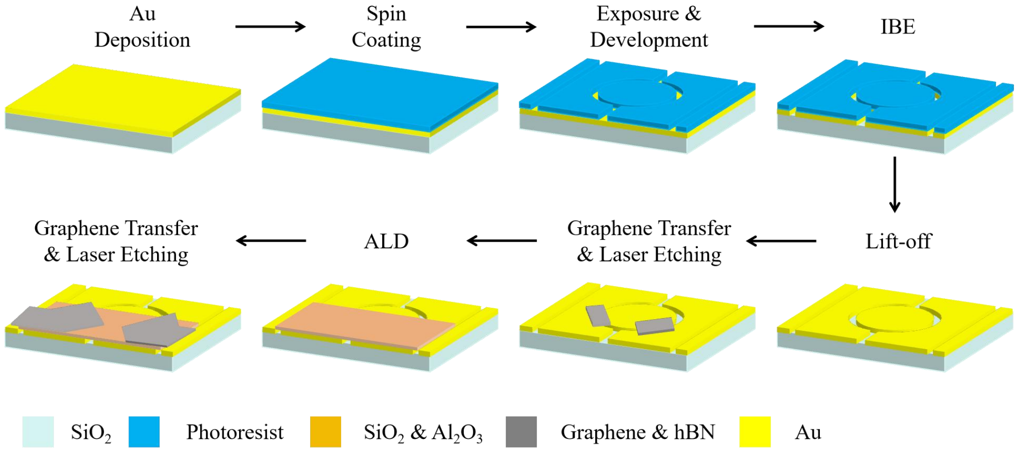

Supplementary Figure S5. Fabrication process of the GIG heterostructure with its corresponding electrodes.

Supplementary Note 5 Measurement of the surface impedance for the GIG heterostructure

The source-drain current as a function of the gate voltage for the GIG heterostructure was evaluated through the utilization of a semiconductor parameter analyzer, and the measured result is shown in Fig. S5(a). With the voltage between the source and drain set to 0.02 V, the source-drain current was observed to increase from 18 μA to 71 μA as the gate voltage was decreased from +4 V to 0 V and subsequently increased negatively to -4 V.

Based on the structural representation depicted in Fig. S3, we estimate the effective area of the bottom graphene layer as a rectangle measuring 135 μm in length and 25 μm in width. According to this approximation, we can calculate the variation of the surface impedance of the bottom graphene layer under different gate voltages from the I-V characteristic curve, which is shown in Fig. S5(b). Since the contact resistance between graphene and the electrode is much smaller than the impedance of graphene, we have neglected the impact of the contact resistance in our calculations.

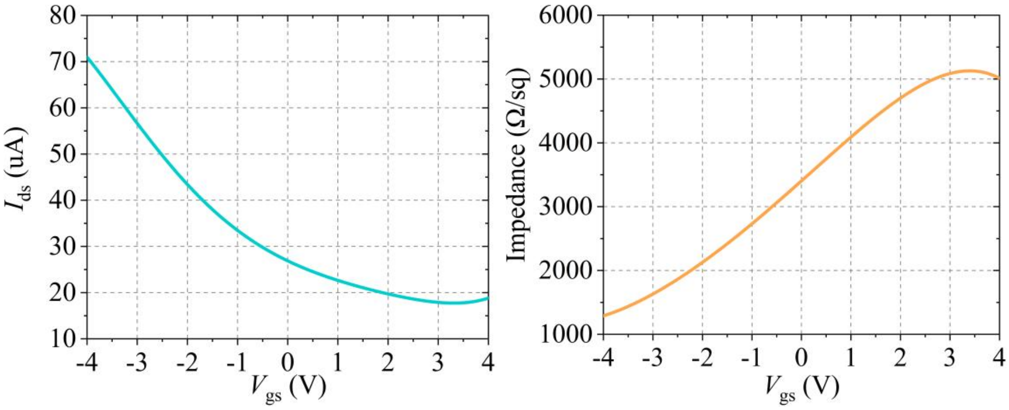

Supplementary Figure S6. a The measured source-drain current as a function of the gate voltage under a source-drain voltage of 0.02V. **b** The corresponding surface impedance of the bottom graphene layer.

Supplementary Note 6 Parameter analysis of the mirror-image operating mode

A. The surface impedance inconsistency of graphene

The tested surface impedance for the bottom graphene layer, as illustrated in Fig. 2(e), is analyzed to determine the impact of graphene inconsistency on the amplitude and phase response of the unit cell. This is demonstrated in Fig. S8 and Fig. S9. In these figures, the subscripts z and y of the S-parameters indicate that the incident electric field is z-polarized, and the transmitted electric field is y-polarized. For the TM_{mn0} mode, the surface impedance of GIG_1 is fixed at 1300 Ω/sq. Upon increasing the surface impedance of GIG_2 from 3700 Ω/sq to 5100 Ω/sq, the transmission amplitude of the TM_{mn0} mode increases by 2 dB, while its transmission phase remains constant. The TM_{nm0} mode exhibits a comparable performance profile. The surface impedance of GIG_1 is fixed at 5100 Ω/sq, and an increase in the surface impedance of GIG_2 from 1200 Ω/sq to 1500 Ω/sq resulted in a 1.5 dB reduction in the transmission amplitude of the TM_{nm0} mode, while the transmission phase remains constant. The analysis corroborates our hypothesis that even if the surface impedance of graphene exhibits inconsistency due to impurity doping or inherent defects, the construction of a working mode with mirror-image induced currents ensures a 180° phase difference between the TM_{mn0} and TM_{nm0} modes over a broad frequency band.

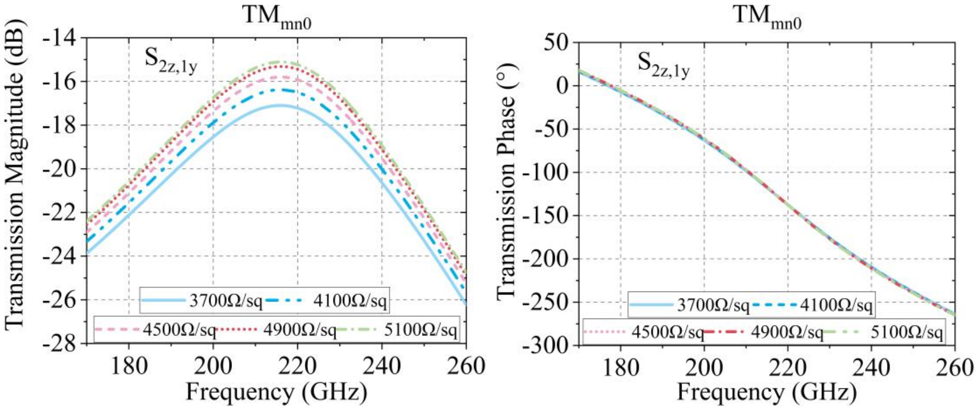

Supplementary Figure S8. Simulated results of the transmission magnitude and phase for TM_{mn0} mode. The surface impedance of GIG_1 is fixed at 1300 Ω/sq, while the surface impedance of GIG_2 varies within the range of 3700-5100 Ω/sq.

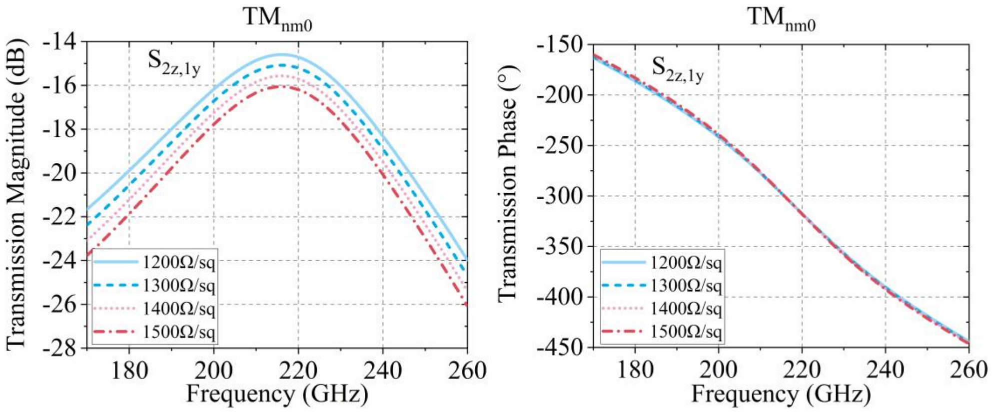

Supplementary Figure S9. Simulated results of the transmission magnitude and phase for TM_{nm0} mode. The surface impedance of GIG_1 is fixed at 5100 Ω/sq, while the surface impedance of GIG_2 varies within the range of 1200-1500 Ω/sq.

B. Thickness of the substrate dielectric slab

We have also analyzed the effect of the thickness of the substrate dielectric slab on the transmission efficiency, as shown in Fig. S10. As the thickness of the dielectric slab is reduced from 300 μm to 150 μm, the maximum transmission amplitude of the TM_{mn0} mode increases by approximately 5 dB. As the thickness of the dielectric slab is further reduced, the transmission efficiency decreases. Considering that a substrate that is too thin is prone to breakage in actual processing, we finally used a quartz substrate with a thickness of 200 μm.

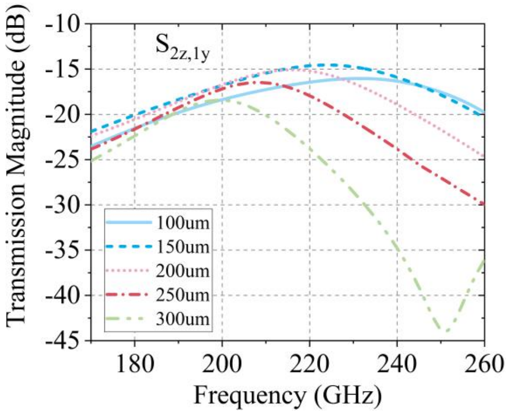

Supplementary Figure S10. Simulated results of the transmission magnitude for TM_{mn0} mode. The surface impedance of GIG_1 and GIG_2 are fixed at 1300 Ω/sq and 5100 Ω/sq, respectively. The height of the substrate varies within the range of 100 to 300 μm.

Supplementary Note 7 Design of beam scanning and its simulation result

A 1-bit column coding method is employed to regulate the beam direction. Despite a relative lower work efficiency compared to 1-bit single-pixel coding, this method is advantageous as it avoids the complex bias circuits and eliminates the need for vertical interconnections and other complex processes, thereby greatly reducing the implementation complexity.[8]

For a horn feed transmissive metasurface, the required transmissive phase for each unit cell is calculated by [9]

$$k \times \left(r_{fmn} - \overline{\mu}_0 \cdot \vec{r}_{mn} \right) + \varphi_{mn} + \varphi_0 = 2n\pi, n = 0, \pm 1, \pm 2, \ldots \tag{S.13}$$

where k is the free space wavenumber, r_{fmn} is the spatial distance between the feed and the mn$^{\text{th}}$ element, φ_0 is a phase constant, $\boldsymbol{\mu}_0$ is the unit vector in the main beam direction, and $\boldsymbol{r}_{mn}$ is the position vector of the mn$^{\text{th}}$ element.

If $\varphi_{\mathrm{mn}} \geqslant 0$, and $\varphi_{\mathrm{mn}} < \pi$, the coding of this unit cell is ‘0’, indicating that the unit cell is operating in $\mathrm{TM}_{\mathrm{mn0}}$ mode. Conversely, if $\varphi_{\mathrm{mn}} \geqslant \pi$, and $\varphi_{\mathrm{mn}} < 2\pi$, the coding of this unit cell is ‘1’, that is, the unit cell is working on $\mathrm{TM}_{\mathrm{nm0}}$ mode. For the column control, the coding of the central row of the unit cell is selected as the coding for the entire column.

The simulation results of the unit cell phase response were used to design of the beam steering performance of the graphene metasurface at a frequency of 210 GHz. The array contains a 12×24 unit cell configuration, forming a 1/16 subarray of the full-scale metasurface. The desired beam direction is achieved by controlling the 0/1 encoding of each column. In the design, a rectangular array configuration is employed in preference to a square or circular array configuration, with the objective of reducing the impact of phase errors from edge units in each column on beam direction and efficiency. A pyramidal horn antenna with vertical polarization is employed for excitation, with a distance of 14 mm between the horn aperture and the metasurface, corresponding to F/D=0.87. The input waveguide of the horn antenna is a WR-4 standard waveguide, with a radiation aperture of 4 mm in both length and width. The simulated gain and radiation pattern at 210 GHz of the horn antenna are presented in Fig. S11. In the frequency range of 170-260 GHz, the antenna gain exhibits an increase from 16.8 dBi to 20.4 dBi.

Fig. S12 illustrates the coding patterns for beam scanning of the metasurface and the corresponding simulated radiation patterns in the *xoy* plane. In accordance with equation (S.13), the corresponding coding patterns have been calculated at the operating frequency of 210 GHz, resulting in the attainment of the main beam directions from 0° to 40°. At the 0° direction, the main beam gain is -5.5 dBi, while the scan loss is less than 3.7 dB within the 40° scanning range.

At present, the side lobes are relatively high and the radiation efficiency is relatively low. This is due to the column coding method and the low transmission rate of the unit cells. Subsequently, more complex encoding methods, such as 2-bit coding, can be employed. Furthermore, attempts can be made to optimize the quality of graphene in order to enhance the transmission rate of the units, thereby achieving lower side lobes and higher radiation efficiency.

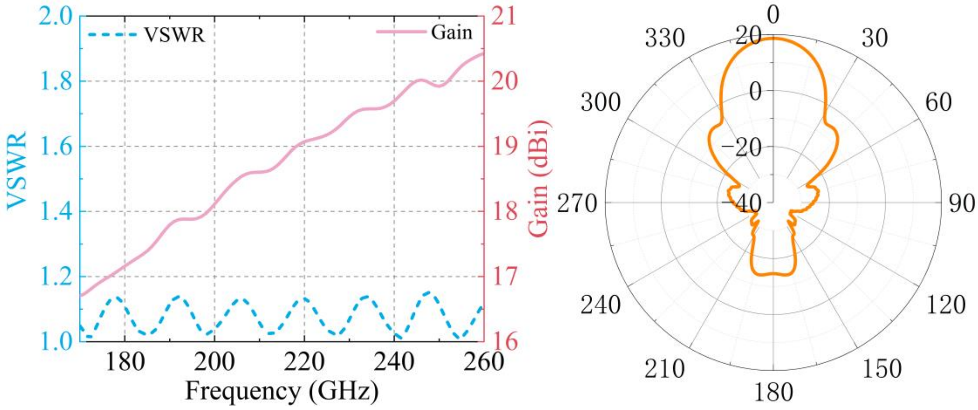

Supplementary Figure S11. Simulated VSWR, gain, as well as the H plane radiation pattern at 210 GHz of the pyramidal horn antenna.

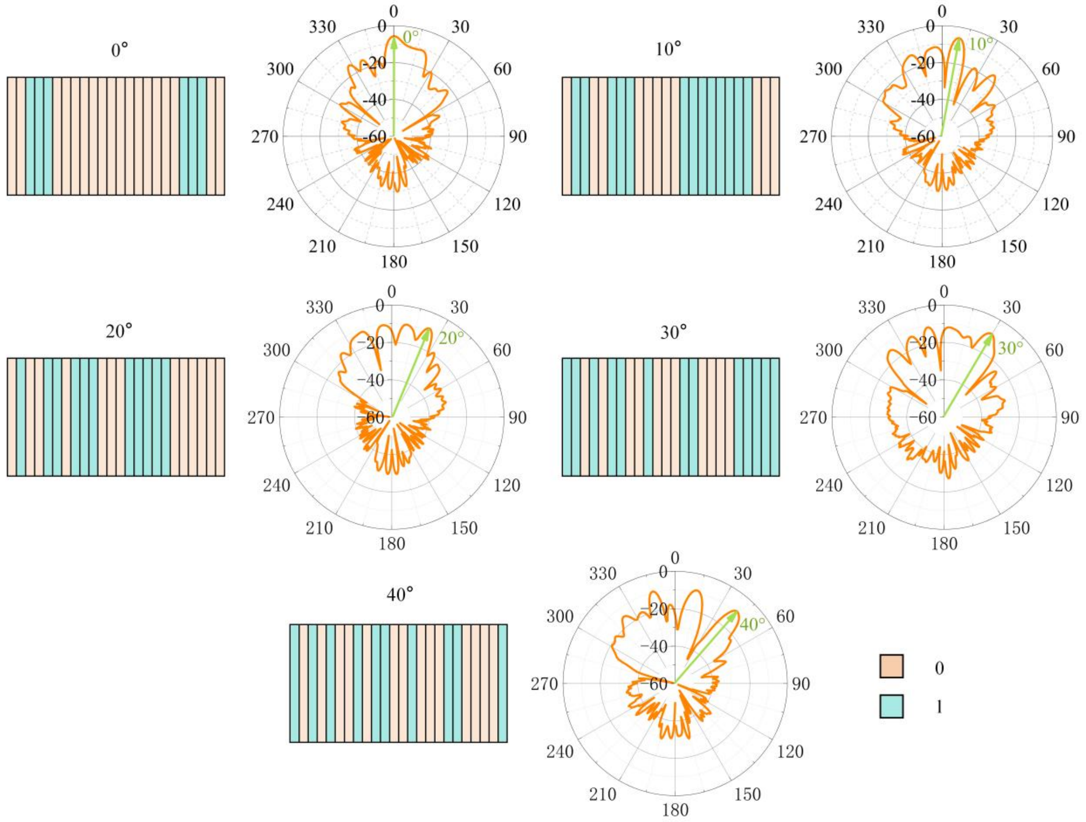

Supplementary Figure S12. Coding patterns and simulated radiation pattern in *xoy* plane of the graphene enabled subscale transmit array.

Supplementary Note 8 Measured results of beam scanning

A vector network analyser (VNA) was employed to assess the radiation characteristics of the antenna in far-field conditions. Port 1 of the VNA is connected to an S-parameter frequency expansion module, which up-converts the signal to a frequency range of 170-260 GHz and excites the graphene metasurface through a horn antenna. The received signal is then captured by another horn antenna, down-converted by the S-parameter frequency expansion module and subsequently input to Port 2 of the VNA. In order to meet the far-field condition, the distance between the graphene metasurface and the receiving horn antenna is 2.6 metres, as illustrated in Fig. S13. The voltage control signal from the programmable power supply, illustrated in Fig. S14, is connected to the PCB control circuit via DC wires, and then connected to the gate electrodes of the metasurface through wire bonding. The drain electrodes of the graphene metasurface are connected to the ground of the programmable power supply. By regulating the output voltage of the programmable power supply, the beam direction of the graphene metasurface can be modified. During the beam scanning test, the supply voltages to the graphene were +1.2V and -1.2V, which correspond to the high and low resistance states of the graphene, respectively.

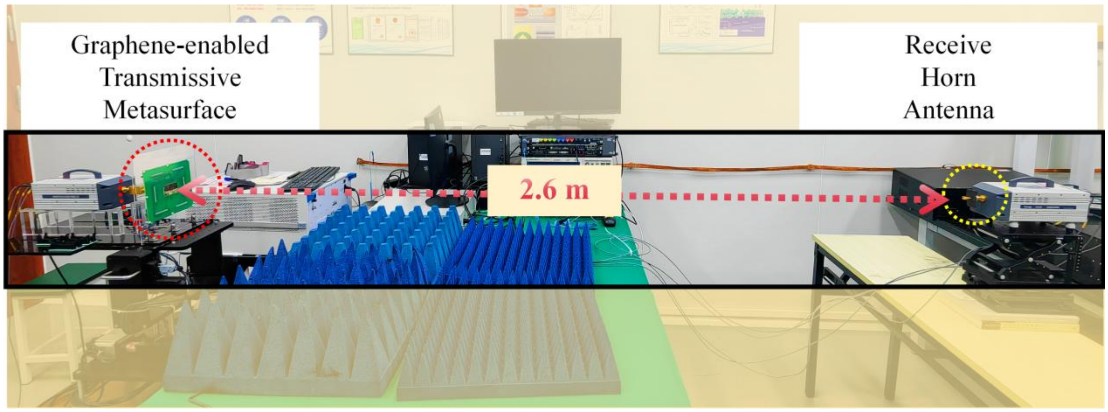

Supplementary Figure S13. Testing environment for the radiation pattern.

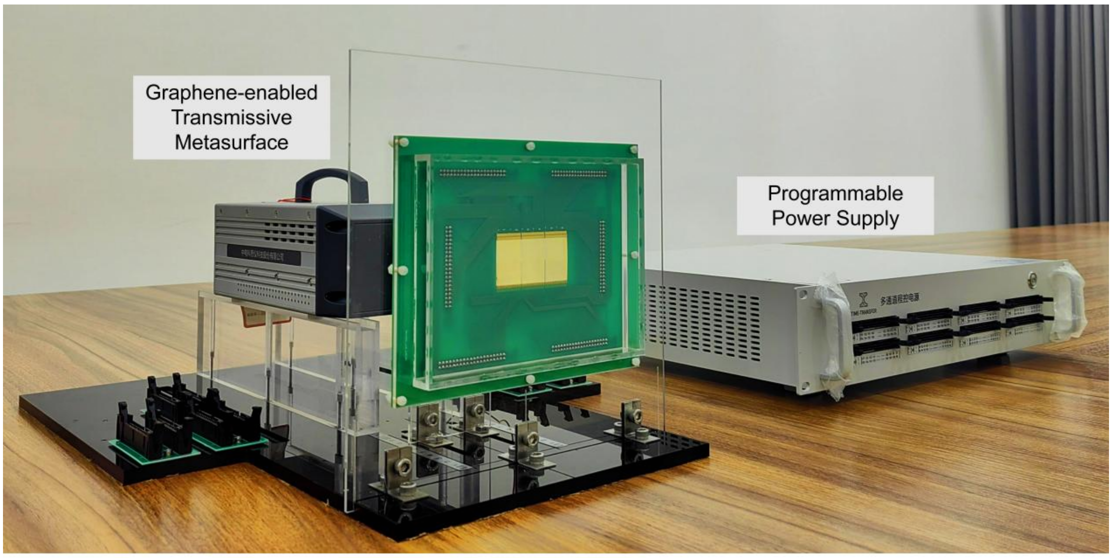

Supplementary Figure S14. Photograph of the Graphene-enabled transmissive metasurface and its programmable power supply.

Fig. S15 depicts the normalized beam scanning performance of the graphene transmissive metasurface at 190GHz, 200GHz, 210GHz, 220GHz, 230GHz, 240GHz, and 250GHz. From the data presented in the figure, it can be observed that at these frequency points, the designed metasurface is capable of achieving ±45° scanning, with a scan loss of no more than 6 dB. The maximum beam pointing deviation is 2.4°, corresponding to the 190 GHz, +5° scan, and the root mean square error of the metasurface beam scanning is 0.75°. Although the current beam scanning efficiency is relatively low, some unit cells may fail during processing, resulting in higher side lobes in the radiation pattern at specific frequencies and angles, the test results nevertheless demonstrate the excellent broadband scanning performance of the graphene transmissive metasurface in the THz frequency band.

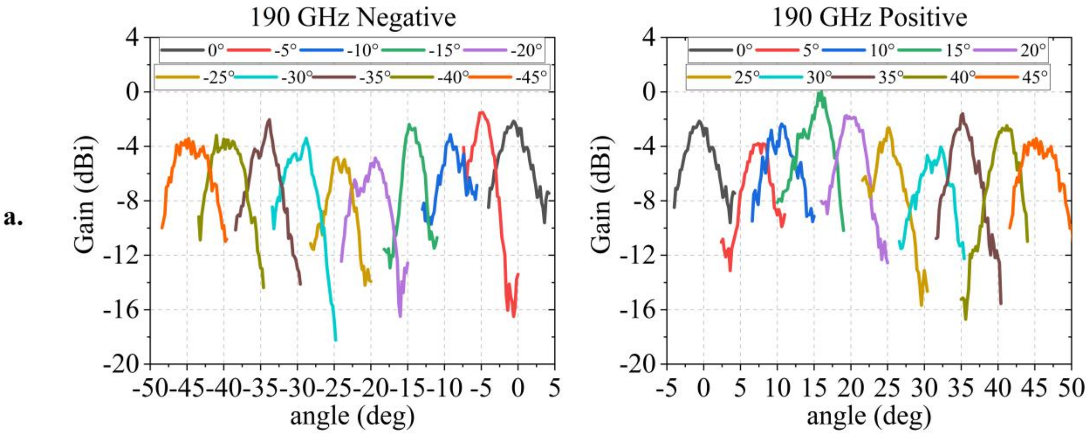

b.

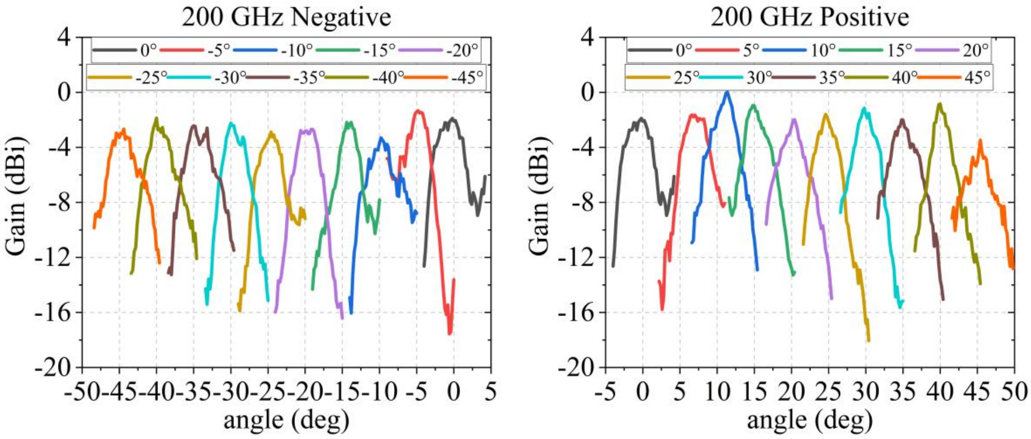
200 GHz Negative
0° -5° -10° -15° -20° -25° -30° -35° -40° -45°
Gain (dBi)
4 0 -4 -8 -12 -16 -20
-50 -45 -40 -35 -30 -25 -20 -15 -10 -5 0 5
angle (deg)
200 GHz Positive
0° 5° 10° 15° 20° 25° 30° 35° 40° 45°
Gain (dBi)
4 0 -4 -8 -12 -16 -20
-5 0 5 10 15 20 25 30 35 40 45 50
angle (deg)

c.

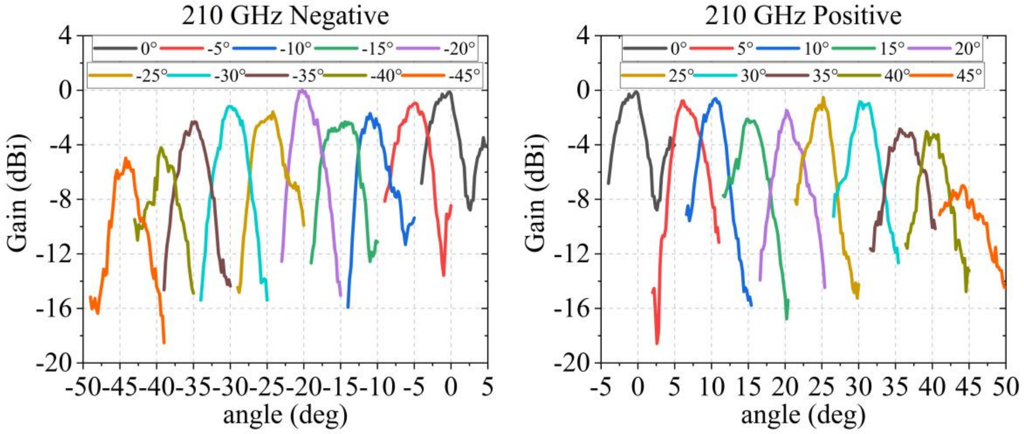
210 GHz Negative
0° -5° -10° -15° -20° -25° -30° -35° -40° -45°
Gain (dBi)
4 0 -4 -8 -12 -16 -20
-50 -45 -40 -35 -30 -25 -20 -15 -10 -5 0 5
angle (deg)
210 GHz Positive
0° 5° 10° 15° 20° 25° 30° 35° 40° 45°
Gain (dBi)
4 0 -4 -8 -12 -16 -20
-5 0 5 10 15 20 25 30 35 40 45 50
angle (deg)

d.

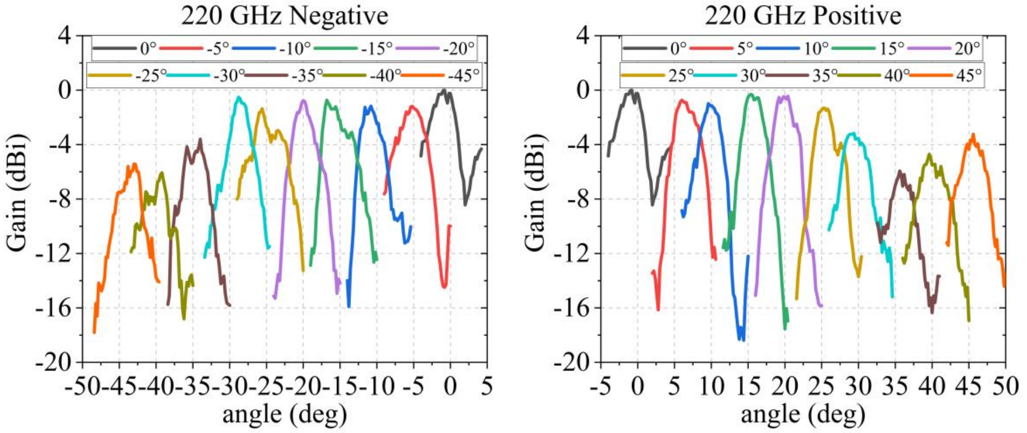
220 GHz Negative
0° -5° -10° -15° -20° -25° -30° -35° -40° -45°
Gain (dBi)
4 0 -4 -8 -12 -16 -20
-50 -45 -40 -35 -30 -25 -20 -15 -10 -5 0 5
angle (deg)
220 GHz Positive
0° 5° 10° 15° 20° 25° 30° 35° 40° 45°
Gain (dBi)
4 0 -4 -8 -12 -16 -20
-5 0 5 10 15 20 25 30 35 40 45 50
angle (deg)

e.

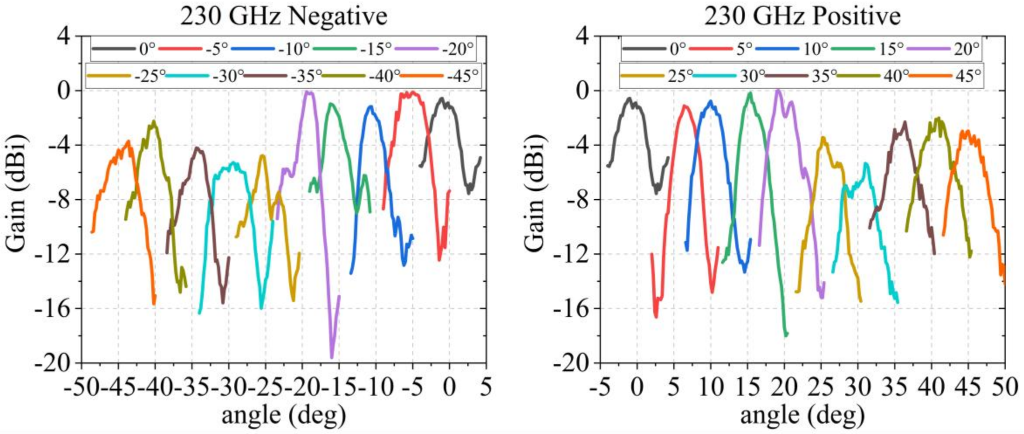
230 GHz Negative
0° -5° -10° -15° -20° -25° -30° -35° -40° -45°
Gain (dBi)
4 0 -4 -8 -12 -16 -20
-50 -45 -40 -35 -30 -25 -20 -15 -10 -5 0 5
angle (deg)
230 GHz Positive
0° 5° 10° 15° 20° 25° 30° 35° 40° 45°
Gain (dBi)
4 0 -4 -8 -12 -16 -20
-5 0 5 10 15 20 25 30 35 40 45 50
angle (deg)

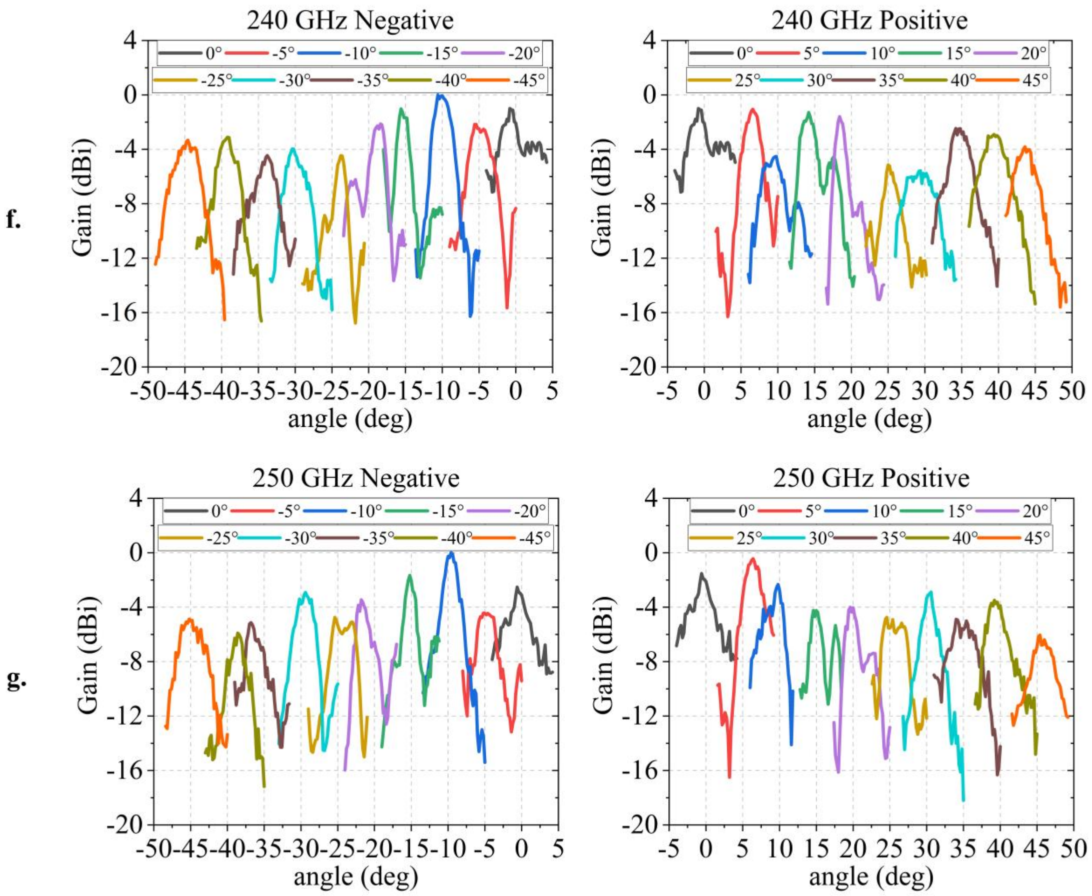

Supplementary Figure S15. Measured beam scanning performance of the graphene-enabled transmissive metasurface at **a** 190 GHz, **b** 200 GHz, **c** 210 GHz, **d** 220 GHz, **e** 230 GHz, **f** 240 GHz, and **g** 250 GHz.

Supplementary Note 9 Measured results of beam gain control

The magnitude of the bias voltage can be employed as a means of controlling the gain of the graphene-enabled metasurface. The gain control characteristics were validated under the 0° beam direction condition at a design frequency of 210 GHz, with the results presented in Figure S16. In the course of the experiment, four groups of bias voltages were set: ±0.6 V, ±0.8 V, ±1.0 V, and ±1.2 V. A negative voltage excites the low resistance state of graphene, while a positive voltage excites the high resistance state. As the absolute value of the bias increases, the gain of the graphene metasurface also increases; the antenna gain increased by 1.5 dB under a bias of 1.2 V compared to 0.6 V. Further optimization of the graphene metasurface process and enhancement of graphene performance can be pursued to achieve a wider gain tuning range.

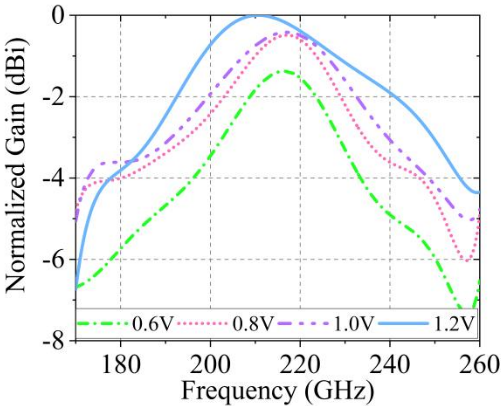

Supplementary Figure S16. Measured result of the gain control performance.

Supplementary Note 10 Comparison of the performance for THz programmable metasurfaces

Table S3 summarizes representative research achievements in the THz metasurface in recent years. Comparative analysis reveals that only Lan et al.'s 2023 study achieved 20% broadband performance, yet its reflective-mode operation limits beam coverage. Most current THz programmable metasurfaces exhibit operational bandwidths below 10%, demonstrating a significant gap from the technical expectations of broadband beam steering required for THz communication and detection systems. Leveraging the ultra-wideband characteristics enabled by graphene's linear energy-momentum relationship, this work achieves an absolute bandwidth of 63 GHz (28.8% relative bandwidth), surpassing the state-of-the-art performance in existing studies.

Supplementary Table S3 Comparison of THz programmable metasurface performance

	type	f_c (GHz)	BW (%)	steering range	active elements
[10]	R	235	4	/	HEMT
[11]	R	265	3.8	±60°	FET
[12]	R	340	20	20°-60°	HEMT
[13]	T	300	< 1	-30°/0°/30°	FET
[14]	T	102.5	9.8	±60°	HEMT
This work	T	218.5	28.8	±45°	Graphene

R: Refletcive, **T**: Transimmive, **HEMT**: High electron mobility transistor, **FET**: Field effect transistor.

Reference

1. Agarwal, H. et al. 2D-3D integration of hexagonal boron nitride and a high-κ dielectric for ultrafast graphene-based electro-absorption modulators. *Nature communications* **12**, 1-6 (2021).
2. Huang, C. et al. Simultaneous control of absorbing frequency and amplitude using graphene capacitor and active frequency-selective surface. *IEEE Transactions on Antennas and Propagation* **69**, 1793-1798 (2020).

3 Jiang, H. et al. Ionic Liquid Loaded Graphene-Based UltraWideband Terahertz Tunable Attenuator. *IEEE Transactions on Microwave Theory and Techniques*, **73**, 1117 - 1125 (2025).

4. Cong, L. et al. Singh R. Fano resonances in terahertz metasurfaces: a figure of merit optimization. *Advanced Optical Materials* **3**, 1537-1543 (2015).
5. Yu, H. et al. A Novel Wideband and High-Efficiency Electronically Scanning Transmitarray Using Transmission Metasurface Polarizer. *IEEE Transactions on Antennas and Propagation* **70**, 3088-3093 (2021).
6. Xi, B. et al. Low-Profile Wideband 1-bit Reconfigurable Transmitarray With 2-D Beam-Scanning Capacity. *IEEE Transactions on Antennas and Propagation* **71**, 3228-3237 (2023).
7. Balci, O. et al. Graphene-enabled electrically switchable radar-absorbing surfaces. *Nature communications* **6**, 6628 (2015).
8. Liu, C. X. et al. Programmable manipulations of terahertz beams by transmissive digital coding metasurfaces based on liquid crystals. *Advanced Optical Materials* **9**, 2100932 (2021).
9. Miao, Z. W. et al. 140 GHz high-gain LTCC-integrated transmit-array antenna using a wideband SIW aperture-coupling phase delay structure. *IEEE Transactions on Antennas and Propagation* **66**, 182-190 (2017).
10. Lynch, J. J. et al. Coded aperture subreflector array for high resolution radar imaging. *Passive and Active Millimeter-Wave Imaging XX. SPIE*, 124-133 (2017).
11. Monroe, N. M. et al. Electronic THz pencil beam forming and 2D steering for high angular-resolution operation: A 98×98-unit 265GHz CMOS reflectarray with in-unit digital beam shaping and squint correction. *2022 IEEE International Solid-State Circuits Conference (ISSCC).* 1-3 (2022).
12. Lan, F. et al. Real-time programmable metasurface for terahertz multifunctional wave front engineering. *Light: Science & Applications* **12**, 191 (2023).
13. VENKATESH, S. et al. A high-speed programmable and scalable terahertz holographic metasurface based on tiled CMOS chips. *Nature Electronics* **3**, 785-793 (2020).
14. Shen, D. et al. Sub-terahertz transmissive reconfigurable intelligent surface for integrated beam steering and self-OOK-modulation. *Light: Science & Applications* **14**, 13 (2025).